

Simulation of scattering from layered spheres with known surface electric field distributions using Mie theory and modified angular spectrum method: Applications to corneal sensing

JOEL LAMBERG^{1,*}, FAEZEH ZARRINKHAT^{1,2}, ALEKSI TAMMINEN¹,
MARIANGELA BAGGIO¹, JUHA ALA-LAURINAHO¹, JUAN RIUS²
JORDI ROMEU², ELSAYED E. M. KHALED^{3,4} AND ZACHARY TAYLOR¹

¹ Department of Electronics and Nanoengineering, MilliLab, Aalto University, Espoo, Finland

² CommSensLab, Technical University of Catalonia/UPC, Barcelona, Spain

³ Department of Electrical Engineering, Assiut University, Assiut, Egypt

⁴ High Institute of Engineering and Technology, Sohage, Egypt

* joel.lamberg@aalto.fi

Abstract: Mie theory is a powerful method to evaluate the scattered fields from the multilayered sphere, where the incident field is expanded to the vector spherical harmonic (VSH) presentation. Then scattered fields are obtained by the T-matrix method. However, obtaining the VSH coefficients for arbitrarily shaped incident fields is difficult and time-consuming. This paper proposes a novel 3D angular spectrum method (3D ASM) for evaluating the VSH coefficients for the incident field, which is defined from the required electric field distribution positioned on the spherical surface. This allows the VSH expansion and evaluation of the scattered fields from a multilayered sphere illuminated with an arbitrary incident wavefront in the Mie Scattering range. This has been computationally challenging with previous methods.

First, the advantage of the beam created with the proposed method compared to the nominal Gaussian beam illumination is addressed with the spherical bandstop filter simulation. Then the incident field computed by the proposed method is compared to the physical-optics simulations showing precise agreement. As an example of the proposed methodology, the cornea is modeled as a multilayered spherical structure, and the scattered fields are computed from the cornea illuminated by the incident field with a spherical top-hat and tapered top-hat wavefronts. Also, the coupling coefficients of the incident and scattered fields from the cornea model are computed in the 200 - 400 GHz frequency range. The results are compared with coupling coefficients obtained with Gaussian beam illumination and referenced to the reflectivity obtained from plane wave illumination on an analog planar structure. The interaction between the layered spherical structures and the spherically matched incident wavefront shows increased agreement with the planar stratified medium theory compared to the Gaussian beam illumination. The method enables more accurate estimations of corneal water content.

© 2022 Optical Society of America under the terms of the [OSA Open Access Publishing Agreement](#)

1. Introduction

Remote sensing of spherical objects with electromagnetic beams has numerous applications in non-destructive evaluation (NDE) [1], biology [2], and medicine [3]. One promising medical application is corneal water content sensing for detection and management of Fuchs's dystrophy and assessment of corneal grafts. Fuchs' dystrophy causes corneal hyperhydration through degradation of the cornea's endothelium and its hydration maintenance functions. Corneal graft rejection is typically preceded by an inflammatory response characterized by increased corneal tissue water content (CTWC) [4]. In both cases, excess corneal water content is usually detected

via visual inspection of diffuse light scattering arising from swollen collagen fibers. In both cases, detection by visually apparent corneal edema is too late in the disease/rejection process to salvage cornea tissue.

Current diagnostic methods restrict *in vivo* CTWC quantification to pachymetry, which infers tissue hydration from thickness quantified via ultrasonic or optical backscatter measurements. However, the mapping from the pachymetry-measured central corneal thickness (CCT) to corneal tissue hydration does not account for physiologic variation and returns significant abnormal hydration for corneal thicknesses off the nominal 580 μm [5].

Recent research suggests that terahertz (THz) systems are suitable for mapping human cornea water content by coupling to the cornea's lossy longitudinal modes [6, 7]. When referenced to THz band wavelengths, the cornea presents as an optically smooth, spherical shell structure with radially varying dielectric properties arising from the water content gradient in the axial dimension [4]. Furthermore, natural physiologic variation in radius of curvature, when referenced to THz band wavelengths, is negligible thus curvature can be assumed and fixed when designing optical systems.

In many reports describing illumination of the cornea, the incident field is modeled as a Gaussian beam in which the radius of curvature (RoC) of the wavefront matches the spherical surface at the optical axis [8,9]. As the focused spot size of the incident field is less than the radius of the cornea, the electromagnetic properties of the cornea can be modeled with stratified media theory (SMT) [10] to capture the dielectric gradient, and effective media theories (EMT) [11] to compute the effective permittivity at a given depth. Application of SMT and EMT implies that a plane wave on a planar film atop an aqueous half-space is a sufficient analogue for spherical cornea under the right illumination. This matching criterion is called the plane-wave condition. Optimization routines can then be applied to estimate corneal water content and thickness from backscattered THz illumination.

However, as the Gaussian beam is observed further from the optical axis, a mismatch between the wavefront and spherical surface increases between the field wavefront and the spherical surface [8], see Figure 1. The phase deviation between the incident wavefront and the desired wavefront matching with the surface of the sphere reduces the theoretical CTWC measurement accuracy when the plane-wave condition and corresponding EMT and SMT are applied. For improved agreement between THz frequency corneal backscatter and that predicted by plane wave based analysis, there is a need to synthesize and simulate a field whose wavefront matches the spherical corneal shape at any point on the surface. In other words, a method that can create the required incident field from an arbitrary, complex electric field distribution initiated at the spherical surface. Furthermore, the method should also be able to model electromagnetic wave interactions between the incident beam and the cornea interior modeled as a multilayered spherical structure that generates complex internal and scattered electric fields from the initial surface distribution. This leads to an inverse imaging problem; first, the optimal wavefront distribution should be created at the cornea's surface, and then the incident beam should be synthesized with the ability to satisfy this surface criterion.

Internal and scattered fields arising from a homogenous sphere with arbitrary, given electric field distributions on the spherical surface can be computed with conventional methods including full-wave simulations, geometrical optics (GO) [12], or physical optics (PO) [13,14]. Conventional methods are also sufficient for calculating propagating fields from source distributions defined on a sphere. These techniques are well studied and accurate given the model fidelity and a suitable wavelength range. However, they cannot assess the internal and scattered electric fields from multilayered spherical objects without considerable computational effort. This problem occurs in full-wave simulation as the volume of the multilayered sphere may require discretization on the order of 10^9 cells, which would exceed available memory on most modern computers. The same discretization and computer memory constraint occurs with the boundary element method,

as each layer boundary should be discretized, to, again, on the order of 10^9 boundary elements. Likewise, geometrical optics is limited to spheres much larger than the illumination wavelength, and ray splitting to accommodate a sufficient number of layers may also exceed available memory. Furthermore, obtaining the steady-state results with physical optics would need tracking of local reflected and transmitted fields from each boundary leading to an immense number of data points and equally infeasible for some computer memory limitations.

The ratio of the corneal radius of curvature (~ 7.8 mm) and THz band wavelengths (~ 3 mm - 0.3 mm) places the problem in the Mie scattering region thus supporting analysis as a pure scattering problem. Mie theory and the generalized Lorentz-Mie theory are powerful methods to evaluate the internal and scattered fields from the multilayered spheres [15]. First, the known incident field is presented in vector spherical harmonics (VSH) expansion which is defined by VSH coefficients [16]. However, obtaining the coefficients for arbitrarily shaped incident fields is difficult [15]. These VSH coefficients for the incident field can be obtained by the angular spectrum (AS) method from the planar surface distributions [17]. The AS method presents the incident field in the angular spectrum domain as the sum of differently oriented plane waves. When this angular summation of the plane waves is presented in a direction cosine coordinate system, it can be used directly to compute the incident VSH coefficients. Then the incident field is expanded to the VSH presentation. Additionally, the internal and scattered fields from a multilayered dielectric sphere can be mapped with the T-matrix method in the Mie scattering region [18]. The limitation of this AS method is that it is nominally compatible with planar interfaces. In [19], the planar AS method was expanded to approximate diffractive fields from 2D curved surfaces. This was obtained by dividing the curved 2D surface into the step-wise subregions windowed by the Gaussian function. This approach was later expanded to the 3D surfaces in [20], where the authors used the same planar step-wise subsections with Gaussian distribution. Both methods approximate well the diffraction, reflections, and transmission from the curved single-layer boundaries, when the RoC is much larger than the wavelength [21]. Thus these methods are not suitable for cornea analysis in the THz region, where the RoC is comparable to the wavelength.

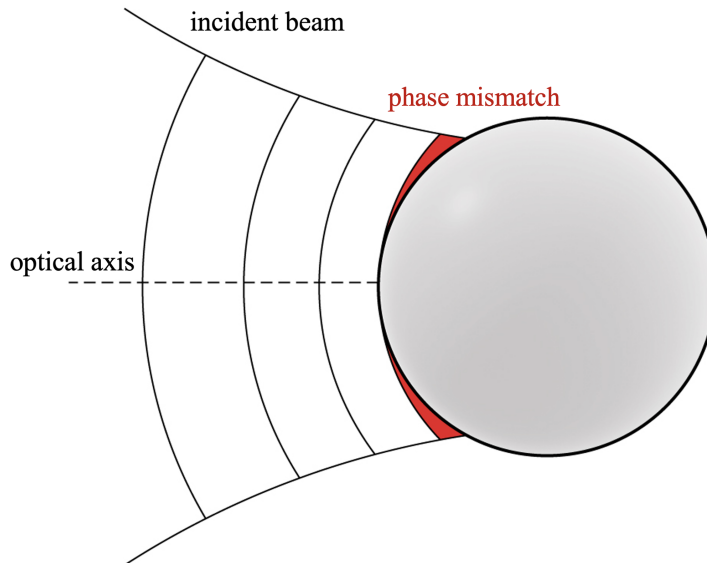


Fig. 1. The incident beam propagating towards the sphere, and the mismatch between the beam wavefront and the spherical surface is proportional to the distance from the optical axis.

In this study, we start with the same approach of dividing the spherical surface into planar subregions. These subregions are presented with equal amplitude, without Gaussian distribution or windowing. Then these subregions are shrunk into infinitesimally small areas, which approach the Dirac's delta function at the limit. This approach gives exact results of the diffractive field from the spherical surface on the limit of infinitesimally small partition. Thus, this study proposes an accurate 3D AS method for the beam synthesis from the spherical surfaces, which can be expanded to arbitrary surfaces taking into account surface structures comparable to the wavelength. Also, with the proposed method the radius of curvature of the surface can be as small as couple of wavelengths. Moreover, this result is equivalent to the angular spectrum presentation of the Stratton-Chu method with magnetic dipole sources [22]. The obtained theory is then utilized to create an incident electric field with the ideal spherical wavefront [23], and the scattered field is calculated from the cornea model with the layered spherical structure of 50 layers.

2. Theory

This work presents the synthesis of the incident electromagnetic field from the arbitrary electric field distribution positioned on the spherical surface with the modified AS method. The method's main idea is that Riemann's surface integral combines differential surface elements, which can be approximated as locally planar elements. Then the radiated field from each element is created with the planar AS method. The total electromagnetic field is the sum of the fields created from the differential sources by the superposition principle [17]. In this approach, we make a physical assumption that when the areas of the elements are small enough, the created field from the differential elements approaches the field from the original surface. This approximation works well for a smooth surface with radius of curvature that is larger than the wavelength.

The derivation starts on an arbitrary point on the unit-sphere, where the spherical components r, θ, ϕ define the surface. These orthogonal spherical components ($\mathbf{e}_r, \mathbf{e}_\theta, \mathbf{e}_\phi$) can be used as base vectors for the local Cartesian coordinate system, whose origin is positioned at the same observation point on the spherical surface. Figure 2 presents the situation, where the spherical components on the surface element are used as base vectors for the local coordinate system. The main steps of the upcoming derivation follow the following structure;

- The relation between the local Cartesian coordinates of each surface element and the global spherical coordinates is derived from the unit-sphere base vectors ($\mathbf{e}_r, \mathbf{e}_\theta, \mathbf{e}_\phi$).
- Each differential element is considered as a field source and the radiated field is presented in the angular domain by the Fourier transform of the electric field distribution.
- The total field is obtained by summing together the fields from the inverse Fourier transform of angular domain presentation.
- Then the total field with polarization vector parallel to the \mathbf{e}_θ is expanded into the VSH presentation.
- Each local coordinate system is presented in the global coordinate system with the origin shift for satisfying the VSH symmetry.
- Finally, the equations of the incident field synthesized from the spherical surface are presented.

After the derivation, the obtained result is proved to be mathematically exact in Appendix A and the result can be generalized to the spheres with arbitrary radii by taking account of the wavelength. Furthermore, the scattered field equations are presented in Appendix B.

2.1. Incident field synthesis

Let us start by defining the base vectors and the relation between coordinate systems. Position vector in standard form is

$$\mathbf{r} = x\mathbf{e}_x + y\mathbf{e}_y + z\mathbf{e}_z, \quad (1)$$

where \mathbf{e}_x , \mathbf{e}_y and \mathbf{e}_z are orthonormal Cartesian base-vectors. Position at unit-sphere is

$$\mathbf{n} = \mathbf{n}(\theta, \phi) = n_x\mathbf{e}_x + n_y\mathbf{e}_y + n_z\mathbf{e}_z, \quad (2)$$

where $|\mathbf{n}| = 1$, and in spherical coordinates $n_x = \sin \theta \cos \phi$, $n_y = \sin \theta \sin \phi$ and $n_z = \cos \theta$.

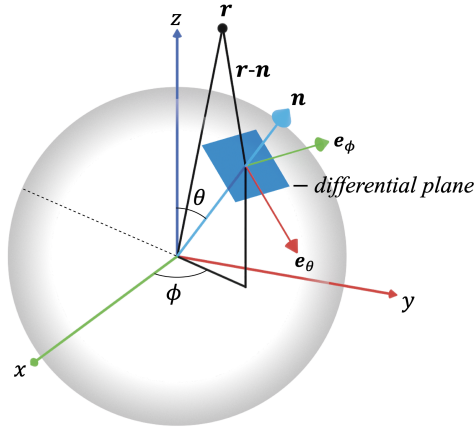


Fig. 2. Global spherical unit-vectors as local Cartesian base-vectors.

The differential surface element on the unit-sphere in spherical coordinates is $d\Omega = \sin \theta d\theta d\phi$. Let the electric field on the segment of the sphere Ω be a continuous function $E_0 = E_0(\theta, \phi)$, $\{0 \leq \theta \leq \theta_0, 0 \leq \phi \leq 2\pi\}$. Let the position \mathbf{r} be fixed and let's observe the electric field at $\mathbf{n}(\theta, \phi)$. The differential field element is considered to be on the plane defined by the unit vectors \mathbf{e}_θ and $-\mathbf{e}_\phi$. Together with their normal $\mathbf{e}_n = -\mathbf{n}$, these determine the right handed orthonormal base $(\mathbf{e}_\theta, -\mathbf{e}_\phi, \mathbf{e}_n)$. Fixing origin at \mathbf{n} this base defines a local coordinate system, where coordinates are denoted by upper-bar like $(\bar{x}, \bar{y}, \bar{z})$. A well known relation between spherical and Cartesian coordinates gives

$$\begin{aligned} \mathbf{e}_\theta &= \frac{d\mathbf{n}}{d\theta} = \cos \theta \cos \phi \mathbf{e}_x + \cos \theta \sin \phi \mathbf{e}_y - \sin \theta \mathbf{e}_z \\ -\mathbf{e}_\phi &= \frac{-1}{\sin \theta} \frac{d\mathbf{n}}{d\phi} = \sin \phi \mathbf{e}_x - \cos \phi \mathbf{e}_y. \end{aligned} \quad (3)$$

The transformation matrix between the coordinates at the base $(\mathbf{e}_\theta, -\mathbf{e}_\phi, \mathbf{e}_n)$ and the coordinates at the standard base $(\mathbf{e}_x, \mathbf{e}_y, \mathbf{e}_z)$, is defined as

$$\Theta(\theta, \phi) = [\mathbf{e}_\theta \ -\mathbf{e}_\phi \ \mathbf{e}_n], \quad (4)$$

where the columns are the vectors \mathbf{e}_θ , $-\mathbf{e}_\phi$ and \mathbf{e}_n . It is an orthonormal matrix, thus $\Theta^T \Theta = I$. The position $\bar{\mathbf{r}}$ in global coordinate system is

$$\bar{\mathbf{r}} = \mathbf{r} - \mathbf{n} = (x - \sin \theta \cos \phi)\mathbf{e}_x + (y - \sin \theta \sin \phi)\mathbf{e}_y + (z - \cos \theta)\mathbf{e}_z. \quad (5)$$

Let's change (5) expressed with respect to the base $(\mathbf{e}_\theta, -\mathbf{e}_\phi, \mathbf{e}_n) : \mathbf{r} - \mathbf{n} = \bar{x}\mathbf{e}_\theta + \bar{y}(-\mathbf{e}_\phi) + \bar{z}\mathbf{e}_n$. By (4) we have position $\bar{\mathbf{r}}$ in local coordinate system as

$$[\bar{x} \ \bar{y} \ \bar{z}]^T = \Theta^T (\mathbf{r} - \mathbf{n}) = \Theta^T [x - \sin \theta \cos \phi \quad y - \sin \theta \sin \phi \quad z - \cos \theta]^T. \quad (6)$$

Let us divide the segment of the sphere Ω containing the electric field distribution to finite partition of small separate sets $\cup_c \Omega_c = \Omega$. Select the point $\bar{\mathbf{n}} = \bar{\mathbf{n}}(\bar{\theta}, \bar{\phi})$ on differential element Ω_c , the vectors associated with it are \mathbf{e}_θ and \mathbf{e}_ϕ . Area Ω_c is projected radially to the plane spanned by the vectors \mathbf{e}_θ and \mathbf{e}_ϕ . The resulting area at the plane is marked as Ω_t . Likewise, function E_0 is projected radially into that plane, limited to set Ω_t and zero elsewhere. This geometry is presented in Figure 3. The resulting restriction is marked as E_0^t . In the local coordinate system it holds $\bar{z} = 0$ on the piece Ω_t , because this is located on the $\bar{x}\bar{y}$ -plane. E_0^t is valid when $\bar{x} \approx 0$ and $\bar{y} \approx 0$. Let the Fourier transform of the function E_0^t on the $\bar{x}\bar{y}$ -plane be

$$A(k_{\bar{x}}, k_{\bar{y}}; \bar{0}) = \mathcal{F} \{E_0^t\} (k_{\bar{x}}, k_{\bar{y}}) = \iint_{\mathbb{R}^2} E_0^t e^{-i(k_{\bar{x}}\bar{x} + k_{\bar{y}}\bar{y})} d\bar{x}d\bar{y}, \quad (7)$$

where $k = |\mathbf{k}| = \sqrt{k_{\bar{x}}^2 + k_{\bar{y}}^2 + k_z^2} = 2\pi/\lambda$. The inverse Fourier transform $\mathcal{F} \{A(k_{\bar{x}}, k_{\bar{y}}; \bar{0})\}$ gives back $E_0^t(\bar{x}, \bar{y}) = E(\bar{x}, \bar{y}, \bar{0})$. Analogously the angular spectrum $A(k_{\bar{x}}, k_{\bar{y}}; \bar{z})$ gives back the desired field $E(\bar{x}, \bar{y}, \bar{z})$ [18], thus

$$E(\bar{x}, \bar{y}, \bar{z}) = \frac{1}{4\pi^2} \iint_{\mathbb{R}^2} A(k_{\bar{x}}, k_{\bar{y}}, \bar{z}) e^{i(k_{\bar{x}}\bar{x} + k_{\bar{y}}\bar{y})} dk_{\bar{x}} dk_{\bar{y}}. \quad (8)$$

The relation between $A(k_{\bar{x}}, k_{\bar{y}}; \bar{0})$ and $A(k_{\bar{x}}, k_{\bar{y}}; \bar{z})$ can be obtained by operating the Helmholtz equation $\nabla^2 E + k^2 E = 0$ to the function (8) [17]. The obtained relation is

$$A(k_{\bar{x}}, k_{\bar{y}}, \bar{z}) = A(k_{\bar{x}}, k_{\bar{y}}; \bar{0}) e^{ik_z |\bar{z}|} = \mathcal{F} \{E_0^t\} (k_{\bar{x}}, k_{\bar{y}}) e^{i|\bar{z}| \sqrt{k^2 - k_{\bar{x}}^2 - k_{\bar{y}}^2}}, \quad (9)$$

where the solution $A(k_{\bar{x}}, k_{\bar{y}}; \bar{z}) = C_\pm e^{\pm ik_z \bar{z}}$ allows both propagation directions $\pm z$ as $e^{ik_z |\bar{z}|}$. Above the angular spectrum theory is locally applied on the local coordinate system to function E_0^t valid on piece Ω_t . Let's observe the field it creates at point $\bar{\mathbf{r}} = \bar{x}\mathbf{e}_\theta + \bar{y}(-\mathbf{e}_\phi) + \bar{z}\mathbf{e}_n$, where the coordinates are as in (6). As shown above, it holds at a fixed point \mathbf{r}

$$E_t(\mathbf{r}) = \frac{1}{4\pi^2} \iint_{\mathbb{R}^2} \mathcal{F} \{E_0^t\} (k_{\bar{x}}, k_{\bar{y}}) e^{i(k_{\bar{x}}\bar{x} + k_{\bar{y}}\bar{y})} e^{i|\bar{z}| \sqrt{k^2 - k_{\bar{x}}^2 - k_{\bar{y}}^2}} dk_{\bar{x}} dk_{\bar{y}}. \quad (10)$$

The total field from the spherical surface is obtained by summing the fields from the differential sources by superposition principle as

$$\begin{aligned} \mathbf{E}_\theta(\mathbf{r}) &\approx \sum_t E_t(\mathbf{r}) \mathbf{e}_\theta = \sum_t \mathbf{e}_\theta \frac{1}{4\pi^2} \iint_{\mathbb{R}^2} \mathcal{F} \{E_0^t\} (k_{\bar{x}}, k_{\bar{y}}) e^{i(k_{\bar{x}}\bar{x} + k_{\bar{y}}\bar{y})} \\ &\times e^{i|\bar{z}| \sqrt{k^2 - k_{\bar{x}}^2 - k_{\bar{y}}^2}} dk_{\bar{x}} dk_{\bar{y}}, \end{aligned} \quad (11)$$

where local coordinates $(\bar{x}, \bar{y}, \bar{z})$ as in (6) and the total field is polarized along the global \mathbf{e}_θ unit-vector. Because the operator $\Delta = \nabla^2$ is linear, the field (11) also satisfies the Helmholtz equation as unit vector \mathbf{e}_θ is locally constant. In order to be precise, if the limit with respect to the areas $|\Omega_t|$ of the sets Ω_t exists, we define mathematically precisely

$$\mathbf{E}_\theta(\mathbf{r}) = \mathbf{E}_\theta(x, y, z) = \lim_{|\Omega_t| \rightarrow 0} \sum_t E_t(\mathbf{r}) \mathbf{e}_\theta. \quad (12)$$

As pointed out at the beginning of the Theory section, this limit also works physically when considering smooth surfaces, and is even more precise when the wavelength decreases compared

to the radius of the sphere. Finally, a further examination is made to obtain a closed-form for the clause (12); we postpone an exact proof at the Appendix A.

Heuristically, when $|\Omega_t|$ is getting smaller, the function $E_0^t/E_0^t(\bar{0}, \bar{0})|\Omega_t|$, normed in volume, is approaching Dirac delta $\delta_{(0,0)}$ in the sense of the distribution theory; $E_0^t/E_0^t(\bar{0}, \bar{0})|\Omega_t| \rightarrow \delta_{(0,0)}$ thus $E_0^t \rightarrow E_0^t(\bar{0}, \bar{0})|\Omega_t|\delta_{(0,0)}$. As known, the Fourier transform of Dirac delta is a constant and equals to 1. Thus, by small $|\Omega_t|$

$$\begin{aligned} \mathcal{F}\{E_0^t\}(k_{\bar{x}}, k_{\bar{y}}) &= \iint_{\mathbb{R}^2} E_0^t e^{-i(k_{\bar{x}}\bar{x}+k_{\bar{y}}\bar{y})} d\bar{x}d\bar{y} \\ &\approx \iint_{\mathbb{R}^2} E_0^t(\bar{0}, \bar{0})|\Omega_t|\delta_{(0,0)} e^{-i(k_{\bar{x}}\bar{x}+k_{\bar{y}}\bar{y})} d\bar{x}d\bar{y} \\ &= E_0(\theta, \phi)|\Omega|\mathcal{F}\{\delta_{(0,0)}\} = E_0(\theta, \phi)|\Omega_t|, \end{aligned} \quad (13)$$

since $E_0(\theta, \phi) = E_0^t(\bar{0}, \bar{0})$ when fixed \mathbf{n} . Then (11) and (13) yield first the form of a Riemann sum, and then an integral as a limit

$$\begin{aligned} \mathbf{E}_\theta(\mathbf{r}) = \mathbf{E}_\theta(x, y, z) &= \lim_{|\Omega_t| \rightarrow 0} \sum_t \mathbf{e}_\theta \frac{1}{4\pi^2} E_0(\theta, \phi)|\Omega_t| \\ &\times \iint_{\mathbb{R}^2} e^{i(k_{\bar{x}}\bar{x}+k_{\bar{y}}\bar{y})} e^{i|\bar{z}|\sqrt{k^2-k_{\bar{x}}^2-k_{\bar{y}}^2}} dk_{\bar{x}}dk_{\bar{y}} \\ &= \frac{1}{4\pi^2} \iint_S E_0(\theta, \phi)\mathbf{e}_\theta(\theta, \phi) \iint_{\mathbb{R}^2} e^{i(k_{\bar{x}}\bar{x}+k_{\bar{y}}\bar{y})} e^{i|\bar{z}|\sqrt{k^2-k_{\bar{x}}^2-k_{\bar{y}}^2}} dk_{\bar{x}}dk_{\bar{y}}d\Omega. \end{aligned} \quad (14)$$

The final form can be written as

$$\mathbf{E}_\theta(\mathbf{r}) = \frac{1}{4\pi^2} \iint_\Omega E_0(\theta, \phi)\mathbf{E}_t(\mathbf{r}; \theta, \phi) \sin\theta d\theta d\phi, \quad (15)$$

where

$$\mathbf{E}_t(\mathbf{r}; \theta, \phi) = \mathbf{e}_\theta(\theta, \phi) \iint_{\mathbb{R}^2} e^{i(k_{\bar{x}}\bar{x}+k_{\bar{y}}\bar{y})} e^{i|\bar{z}|\sqrt{k^2-k_{\bar{x}}^2-k_{\bar{y}}^2}} dk_{\bar{x}}dk_{\bar{y}} \quad (16)$$

and \bar{x}, \bar{y} and \bar{z} are as in (6). It is worthwhile to mention that equation (16) is similar to the $\mathbf{E}_t = -\nabla \times (\mathbf{M}G)$ after replacing the scalar Green's function G by its angular spectrum given by Weyl identity, where $\mathbf{M} = -2\mathbf{n} \times \mathbf{e}_\theta$ is a small magnetic dipole [24]. This leads equation (15) to be a particular case of the Stratton-Chu equation for electric field in which only the magnetic sources $\mathbf{M} = -\mathbf{n} \times \mathbf{E}_{surf}$ are presented and the electric ones $\mathbf{J} = \mathbf{n} \times \mathbf{H}_{surf}$ have been removed [25].

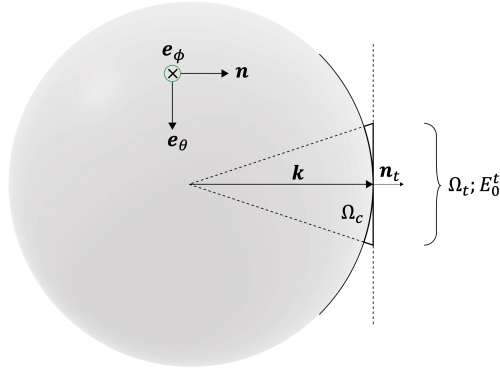


Fig. 3. Spherical segment Ω_c projected into a plane Ω_t .

2.2. Polarization

In the derived equation (15), the electric field component is along \mathbf{e}_θ at the spherical surface, creating a globally continuous polarization. The polarization of each differential source is selected on $\bar{x}\bar{z}$ -plane at source's local coordinate system. Let us consider function (16), with the electric field along \mathbf{e}_θ

$$\mathbf{E}_t(\bar{x}, \bar{y}, \bar{z}) = \mathbf{e}_\theta \iint_{\mathbb{R}^2} e^{i\bar{\mathbf{k}} \cdot \bar{\mathbf{r}}_{||}} dk_{\bar{x}} dk_{\bar{y}}, \quad (17)$$

where $\bar{\mathbf{r}}_{||} = (\bar{x}, \bar{y}, |\bar{z}|)$. Equation (17) will give us the local \bar{x} -component of the electric field. The local \bar{z} -component for the polarization is obtained from $\mathbf{E}_t \cdot \bar{\mathbf{k}} = E_{\bar{x}}k_{\bar{x}} + E_{\bar{y}}k_{\bar{y}} + E_{\bar{z}}k_{\bar{z}} = 0$ for each plane wave [26]. Because of polarization on the $\bar{x}\bar{z}$ -plane as mentioned above, we have $E_{\bar{y}} = 0$ and

$$E_{\bar{z}} = -\left(\frac{k_{\bar{x}}}{k_{\bar{z}}}\right)E_{\bar{x}}. \quad (18)$$

The final form of (17) is obtained as

$$\mathbf{E}_t(\bar{x}, \bar{y}, \bar{z}) = \iint_{\mathbb{R}^2} e^{i\bar{\mathbf{k}} \cdot \bar{\mathbf{r}}_{||}} \left[\mathbf{e}_{\bar{x}} - \left(\frac{k_{\bar{x}}}{k_{\bar{z}}}\right) \mathbf{e}_{\bar{z}} \right] dk_{\bar{x}} dk_{\bar{y}}, \quad (19)$$

where $\mathbf{e}_{\bar{x}} = \mathbf{e}_\theta$, $\mathbf{e}_{\bar{y}} = -\mathbf{e}_\phi$ and $\mathbf{e}_{\bar{z}} = \mathbf{e}_n = -\mathbf{n}$ as defined in (2) and (3). The total polarization at the spherical surface is thus in line with the orthodrome lines between the poles of the sphere, and creates a desired polarization when the middle point of the segment Ω is located at the $\theta = \pi/2$. The function (19) is integrated over the real disk $k_{\bar{x}}^2 + k_{\bar{y}}^2 \leq k^2$ for obtaining only propagating waves and those waves outside of the disk are evanescent. Using direction cosine coordinate system, the above equation can be written as [18]

$$\mathbf{E}_t(\bar{x}, \bar{y}, \bar{z}) = k^2 \int_0^\pi \sin \xi \left\{ \int_0^\pi \mathbf{e}_0(\xi, \zeta) e^{ik(\bar{\mathbf{s}} \cdot \bar{\mathbf{r}}_{||})} \sin \zeta d\zeta \right\} d\xi, \quad (20)$$

where ξ and ζ are direction cosines related to spherical coordinates as $\xi = \cos^{-1}(\sin \theta \cos \phi)$ and $\zeta = \cos^{-1}(\sin \theta \sin \phi)$. The polarization \mathbf{e}_0 in terms of direction cosines is given as

$$\mathbf{e}_0(\xi, \zeta) = \mathbf{e}_{\bar{x}} - \frac{\cos \xi}{(1-s^2)^{1/2}} \mathbf{e}_{\bar{z}}. \quad (21)$$

Additionally $s^2 = \cos^2 \xi + \cos^2 \zeta$, and the vector $\bar{\mathbf{s}}$ is

$$\bar{\mathbf{s}} = \cos \xi \mathbf{e}_{\bar{x}} + \cos \zeta \mathbf{e}_{\bar{y}} + (1-s^2)^{1/2} \mathbf{e}_{\bar{z}}. \quad (22)$$

2.3. VSH expansion and origin shift

The total incident electric field from the spherical surface distribution is obtained from the formula (15). When (16) is expanded to the vector spherical harmonics, the origin of the local coordinate system needs to be shifted to the global origin due to the spherical symmetry of the VSH presentation. This means that the dielectric spheres in each local coordinate system will be centered on the local origin, i.e., at the surface. Thus each local spherical object needs to be shifted to the global origin while the position of the surface source is kept fixed. This is done by first shifting the local origins to the global origins and then shifting the positions of the differential source elements back to the original places. After this procedure, each local source element is presented in the global coordinate system with the ability to add the dielectric sphere to the right location. To do so, equation (20) is evaluated by numerical integration over a disk of radius k using the trapezoidal rule with uniform-width l [18]

$$\mathbf{E}_{t_{ij}} \approx p^2 \sum_i \sin \xi_i \sum_j \sin \zeta_j \mathbf{e}_{0_{ij}}(\xi_{t_i}, \zeta_{t_j}) e^{ik(\bar{\mathbf{s}}_{ij} \cdot \bar{\mathbf{r}}_{||})}, \quad (23)$$

where the indices i and j refers to plane waves with propagation constants k_x^i and k_y^j respectively to \bar{x} and \bar{y} directions. $p = \xi_{t+1} - \xi_t = \zeta_{t+1} - \zeta_t$ is the step-size of the numerical integration. Integration limit of radius k is selected, because the electric field outside that area is rapidly decreasing. The trapezoidal rule method is highly accurate on periodic functions [27], such as equation (20). The transformation matrix from $(\bar{x}\bar{y}\bar{z})$ to (xyz) is $\Theta(\theta, \phi)$ as in (4). We want to express the dot product $\bar{\mathbf{s}}_{ij} \cdot \bar{\mathbf{r}}_{||}$ in the global coordinates. Let's write $\bar{\mathbf{r}} = (\bar{x}, \bar{y}, \bar{z})$. We have a simple connection $\mathbf{r} - \mathbf{n} = \Theta \bar{\mathbf{r}}$ as in (6); that will be used. So we define $\bar{\mathbf{s}}_{ij}^{||} = \bar{\mathbf{s}}_{ij}$, when $\bar{z} > 0$, but, when $\bar{z} < 0$, the sign of \bar{z} -coordinates in $\bar{\mathbf{s}}_{ij}$ is exchanged. Consequently, we can write $\bar{\mathbf{s}}_{ij} \cdot \bar{\mathbf{r}}_{||} = \bar{\mathbf{s}}_{ij}^{||} \cdot \bar{\mathbf{r}}$. Let us define

$$\mathbf{s}_{ij} = \Theta \bar{\mathbf{s}}_{ij}^{||}. \quad (24)$$

As a result we get

$$\begin{aligned} \bar{\mathbf{s}}_{ij} \cdot \bar{\mathbf{r}}_{||} &= \bar{\mathbf{s}}_{ij}^{||} \cdot \bar{\mathbf{r}} = \bar{\mathbf{s}}_{ij}^{||} \cdot \Theta^T (\mathbf{r} - \mathbf{n}) = \Theta \bar{\mathbf{s}}_{ij}^{||} \cdot (\mathbf{r} - \mathbf{n}) \\ &= \mathbf{s}_{ij} \cdot (\mathbf{r} - \mathbf{n}) = \mathbf{s}_{ij} \cdot \mathbf{r} - \mathbf{s}_{ij} \cdot \mathbf{n}. \end{aligned} \quad (25)$$

Based on (25), the term $e^{ik(\bar{\mathbf{s}}_{ij} \cdot \bar{\mathbf{r}}_{||})}$, which is in the local coordinate system, can be presented in the global coordinate system as

$$e^{ik(\bar{\mathbf{s}}_{ij} \cdot \bar{\mathbf{r}}_{||})} = e^{ik(\mathbf{s}_{ij} \cdot \mathbf{r})} e^{-ik(\mathbf{s}_{ij} \cdot \mathbf{n})}, \quad (26)$$

where $e^{-ik(\mathbf{s}_{ij} \cdot \mathbf{n})}$ presents the shift of beam waist of the differential source from global origin to the unit-sphere surface. Now each plane wave in the angular spectrum created from the differential source is presented in a global coordinate system. The total incident electric field is obtained as the sum of the plane waves in the angular spectrum, and at an arbitrary point \mathbf{r} in space expressed by VSHs can be written as [18]

$$\begin{aligned} \mathbf{E}_t(k\mathbf{r}) &= p^2 \sum_m \sum_n D_{mn} \left[a_{\text{emn}}^t \mathbf{M}_{\text{emn}}^1(k\bar{\mathbf{r}}) + a_{\text{omn}}^t \mathbf{M}_{\text{omn}}^1(k\bar{\mathbf{r}}) \right. \\ &\quad \left. + b_{\text{emn}}^t \mathbf{N}_{\text{emn}}^1(k\bar{\mathbf{r}}) + b_{\text{omn}}^t \mathbf{N}_{\text{omn}}^1(k\bar{\mathbf{r}}) \right], \end{aligned} \quad (27)$$

where $D_{mn} = \frac{\epsilon_m(2n+1)(n-m)!}{4n(n+1)(n+m)!}$ is a normalization factor. ϵ_m is equal to 1 for $m = 0$ and is equal to 2 for $m > 0$. $\mathbf{M}_{\text{emn}}^1$, $\mathbf{M}_{\text{omn}}^1$, $\mathbf{N}_{\text{emn}}^1$ and $\mathbf{N}_{\text{omn}}^1$ are the VSH of the first kind and a_{emn}^t , a_{omn}^t , b_{emn}^t and b_{omn}^t are incident beam expansion coefficients given as

$$\begin{aligned} a_{\text{emn}}^t &= \sum_i \sin \xi_i \sum_j \sin \zeta_j a_{\text{emni}_j}^t e^{-ik(\mathbf{s}_{ij} \cdot \mathbf{n})}, \\ a_{\text{omn}}^t &= \sum_i \sin \xi_i \sum_j \sin \zeta_j a_{\text{omni}_j}^t e^{-ik(\mathbf{s}_{ij} \cdot \mathbf{n})}, \\ b_{\text{emn}}^t &= \sum_i \sin \xi_i \sum_j \sin \zeta_j b_{\text{emni}_j}^t e^{-ik(\mathbf{s}_{ij} \cdot \mathbf{n})}, \\ b_{\text{omn}}^t &= \sum_i \sin \xi_i \sum_j \sin \zeta_j b_{\text{omni}_j}^t e^{-ik(\mathbf{s}_{ij} \cdot \mathbf{n})}. \end{aligned} \quad (28)$$

The VSH coefficients for each ij - plane wave $a_{\text{emni}_j}^t$, $a_{\text{omni}_j}^t$, $b_{\text{emni}_j}^t$ and $b_{\text{omni}_j}^t$ are defined in Appendix B. The equation for the incident field (15), adapted by polarization (19), can also be written in vector spherical expansion (27) as

$$\mathbf{E}(\mathbf{r})_{\text{inc}} = \frac{1}{4\pi^2} \iint_{\Omega} E_0(\theta, \phi) \mathbf{E}_t(k\mathbf{r}; \theta, \phi) \sin \theta d\theta d\phi. \quad (29)$$

A similar scattered field presentation mapped with the T-matrix method is presented as

$$\mathbf{E}(\mathbf{r})_{sca} = \frac{1}{4\pi^2} \iint_{\Omega} E_0(\theta, \phi) \mathbf{E}_{scat}(k\mathbf{r}; \theta, \phi) \sin \theta d\theta d\phi, \quad (30)$$

where \mathbf{E}_{scat} is introduced in Appendix B.

3. Results

Now we present three different simulation scenarios, and they are: 1) Incident field simulations and comparison to similar physical optics simulations, to validate the accuracy of the field synthesis. 2) The spherical bandstop filter simulations to verify the benefits of the proposed method. 3) The cornea simulations to confirm the increased accuracy of cornea's thickness and water content analysis.

3.1. Incident field simulations

First, the incident electric field was synthesized from the top-hat field distribution positioned on the spherical surface with Fibonacci sampling using a derived equation (29). This field has a matching wavefront at the spherical surface, with the main polarization along the \mathbf{e}_θ direction. The incident field was evaluated at the plane transverse to the propagation x-axis at 40 mm from the origin of the sphere. The position of the evaluation plane along the propagation axis can be changed without restraints. In our case, the evaluation plane location is selected to match the approximated location of the lens in a quasioptical system. At this distance, the converging beam can be focused with reasonably small focusing elements. Also, this location is identical to the lens location in a future quasioptical system, designed to create the desired field distribution matching the spherical surface. All the following simulations were realized with a constant electric field within subtended angle of 30° on the spherical surface and the transverse evaluation plane at the yz-plane, see Figure 4. The only exception is shown in Figure 8, where the evaluation plane is along the xy-plane.

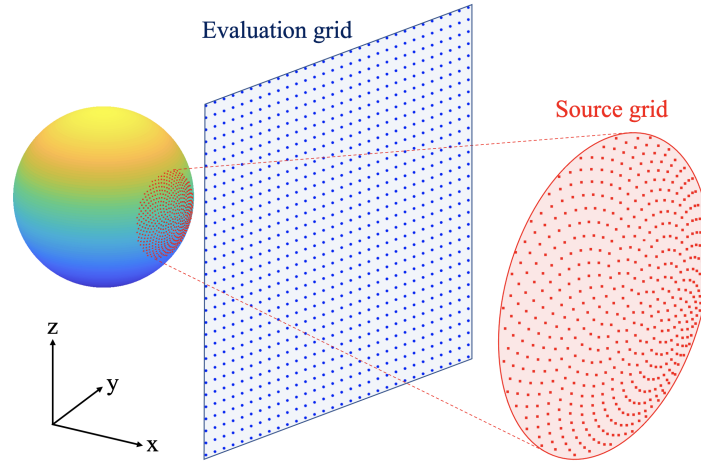


Fig. 4. The simulation arrangement of beam propagation between the spherical surface and evaluating plane, where evaluating plane is marked as blue dots. This plane has $100 \times 100 \text{ mm}^2$ area, located at $x = 40 \text{ mm}$ from the origin of the sphere. The source grid with 681 Fibonacci distributed differential sources is marked as red dots at the spherical surface and at the enlargement of the surface grid. The subtended angle of the spherical cap enclosing the differential source grid is 30° .

Then the Cartesian components of the incident field (E_{3DASM}) calculated by the proposed

method were compared to the identical physical-optics simulation (E_{PO}) at 175 GHz frequency. The comparison provides precise matching down to less than a -41 dB average difference in amplitude and less than 1° average difference in phase, see Figure 5. This difference was calculated for each component as $\|E_{3DASM} - E_{PO}\|_{ave}$ for the amplitude and $\|\angle E_{3DASM} - \angle E_{PO}\|_{ave}$ for the phase. The magnitude and phase components of the electric field computed by the physical-optics are visually identical to the E_{3DASM} results, thus they are not plotted.

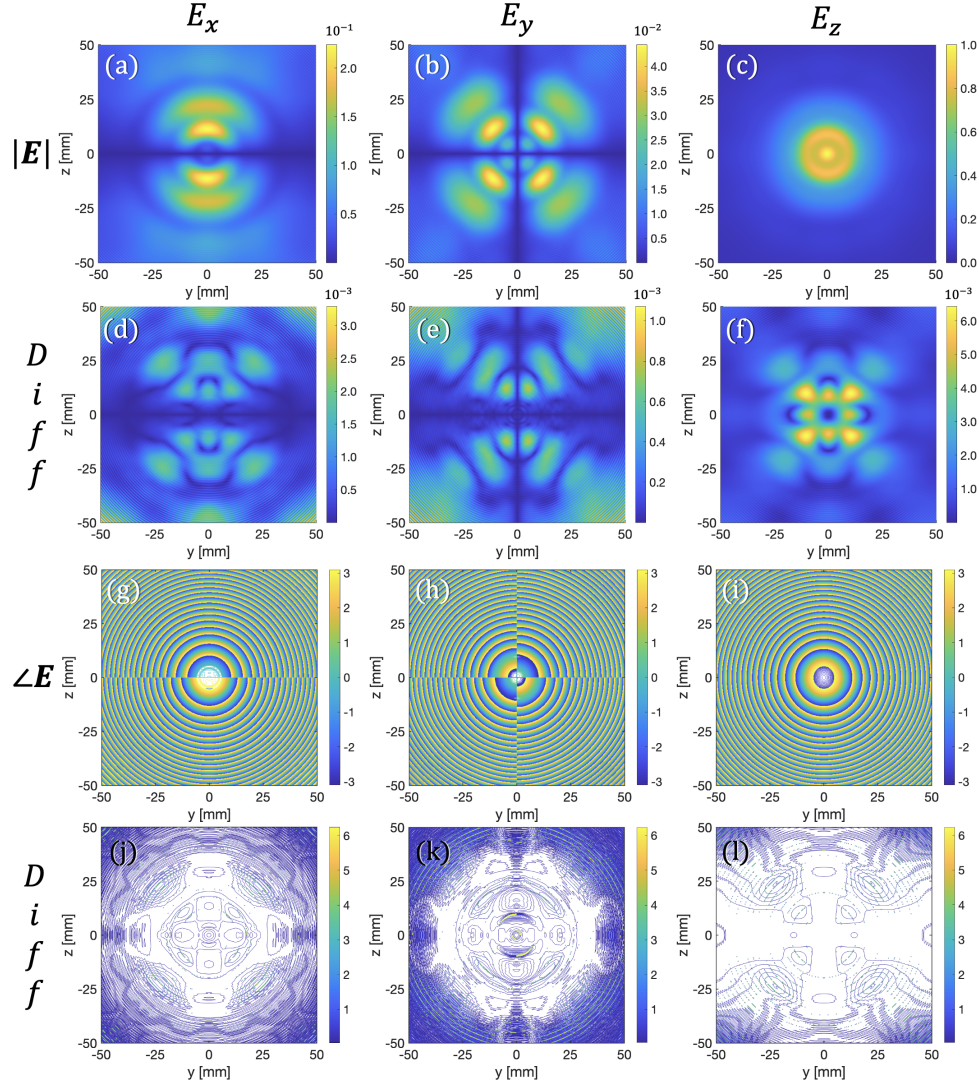


Fig. 5. Subfigures a)-c) are the magnitudes of the electric field components computed by the proposed 3D ASM method, and d)-f) are the magnitude differences between the 3D ASM and PO method at 175 GHz. Subfigures g)-i) are the phases of the electric field components computed by the proposed 3D ASM method, and j)-l) are the phase differences between the 3D ASM and PO method at 175 GHz.

3.2. Bandstop filter backscatter simulations

After the simulation verification of the incident field, let's investigate the analogy of the spherical layered structure compared to the planar layered structure, see Figure 6. To compare these structures properly, we must take into account two different scenarios. When the spherical layered structure has a lossless core, it creates a cavity with multiple internal reflections inside the core. Then the analog planar structure is presented in subfigure 6 b). If the spherical layered structure has a lossy core to prevent the internal reflection in the core, the analog planar structure is presented in subfigure 6 c).

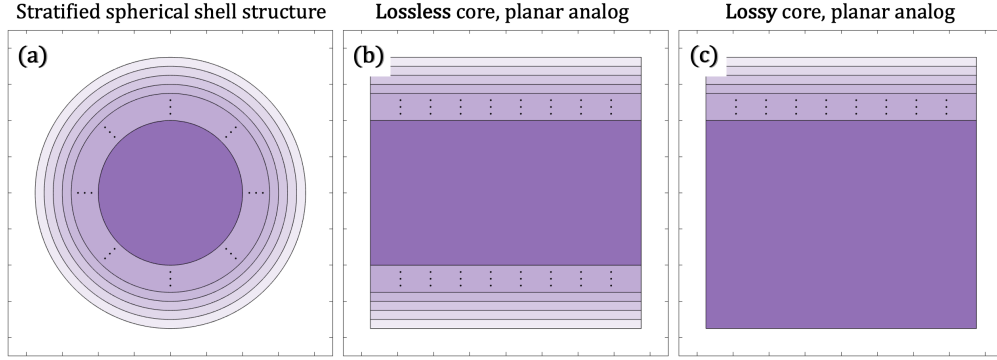


Fig. 6. Subfigure **a**) is stratified spherical shell structure, subfigure **b**) presents the analog planar structure when the spherical structure have a lossless core, and subfigure **c**) presents the analog planar structure when the spherical structure have a lossy core.

Then, the benefits of illuminating spherical layered structures with the beam with a spherically matching wavefront compared to the Gaussian beam are presented. This is done by reproducing a planar 27-layer bandstop filter to an analog spherical structure. The original filter is 3627 nm thick with alternating layers of TiO_2 and SiO_2 , with refractive indexes of 2.5 and 1.45 respectively [28]. A spherically analog structure was created with a 4000 nm radius sphere with a lossless and lossy ($\epsilon = 1 - 0.5i$) core to prevent the internal reflections. Then spherical bandpass filter was illuminated in the 450 - 700 nm wavelength range by a normal and tapered top-hat beam created by the proposed 3D ASM method and by Gaussian beam with different beam size and position scenarios presented in [29, 30]. These results are compared to the plane wave illumination of the similar planar filter structures in Figure 7.

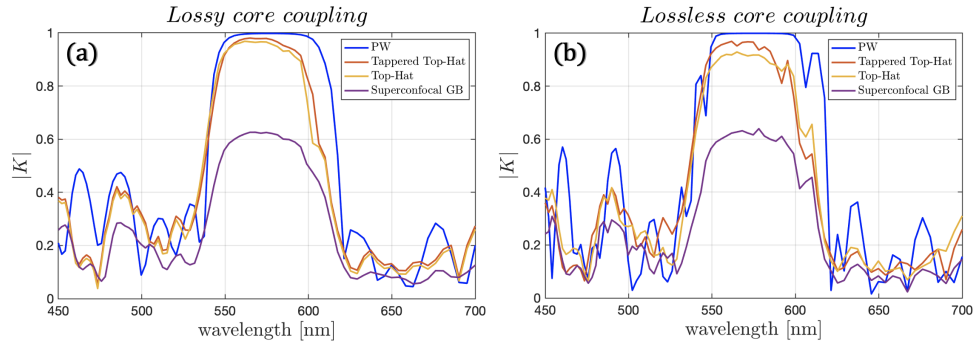


Fig. 7. Coupling coefficients from the spherical layered filter model, where **a**) presents the lossy core with $\epsilon = 1 - 0.5i$ permittivity and **b**) presents the lossless core scenario.

In this simulation example, the spherical layers extend the entire radius of the sphere from the surface to the core, allowing the beam to disperse as it propagates to the deepest layers. This phenomenon produces a small difference between the planar stratified medium theory model with PW illumination and the model of the spherical structure with converging beam illumination. Nevertheless, the simulation shows an increased and relatively well-matched coupling coefficient (K) between the incident and scattered fields with normal and tapered top-hat beams compared to the superconfocal Gaussian beam illumination. The formula for computing K is presented in Appendix B.

3.3. Cornea backscatter simulations

The cornea is the transparent front part of the eye covering the iris, pupil, and anterior chamber. The water percentage of the cornea increases gradually from the anterior surface to the posterior surface. Thus, the permittivity of the cornea differs radially and can be modeled by the spherical multilayered structure. The cornea was modeled as a 7.8 mm radius sphere with a 580 μm thick multilayered spherical shell structure with a pure-water core. The permittivity gradient of the cornea was modeled with 50 layers. Each layer's permittivity was obtained with the effective medium theory via the Bruggeman model [31], and the permittivity of the pure-water core was calculated by the double-Debye model [32]. The corneal shell consisted of 40 % water on the anterior surface and 70 % water on the posterior surface. The cornea is modeled as relatively thin layered structure compared to the radius of the sphere. Due to this, the propagating beam does not disperse as much as in the bandpass filter and the difference between the scattering from planar and spherical structure is decreased. First, the total field $\mathbf{E}_{tot} = \mathbf{E}_{inc} + \mathbf{E}_{scat}$, including the scattered field from the 50-layer cornea model was simulated in the plane along the propagation axis at 175 GHz frequency. This is done for illustrating the beam behavior and the equal phase wavefront on the spherical surface, where the internal field \mathbf{E}_{int} is not plotted, see Figure 8. The scattered field was calculated by the formula (49) from Appendix B. It's worthwhile to mention that the 3D ASM method has no singularities at the source points due to its eigenfunction nature, and the incident and scattered fields can be evaluated at the source points as well. The source points are included in Figure 8 at the spherical surface.

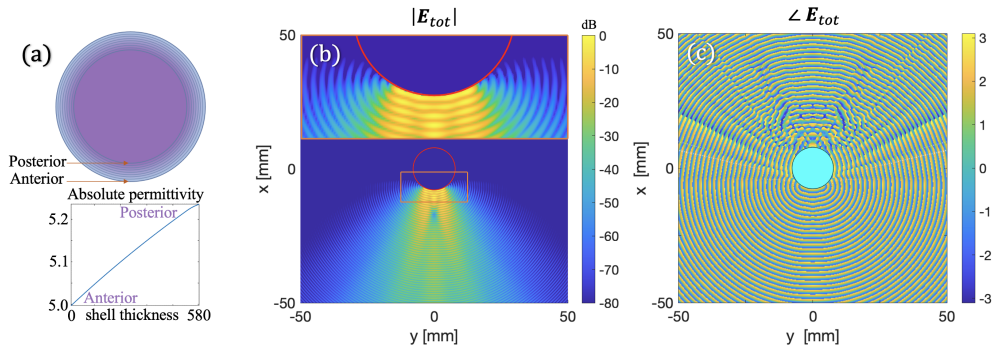


Fig. 8. **a)** presents the radially changing permittivity of the cornea shell, **b)** is amplitude (dB) and **c)** is phase (rad) of the total electric field outside the cornea at xy -plane at 175 GHz. The cornea is represented with a red circle. The top part in **b)** shows a zoom-in plot in the vicinity of the cornea marked with the rectangle in the lower part of the red circle.

Each Cartesian component of the scattered field from the same cornea model was computed at the transverse evaluation plane arrangement, introduced in the Figure 4. The components are normalized by the main polarization E_z -component of the incident field from the Figure 5 (c).

The change in amplitude distribution of the scattered field compared to the incident field is in

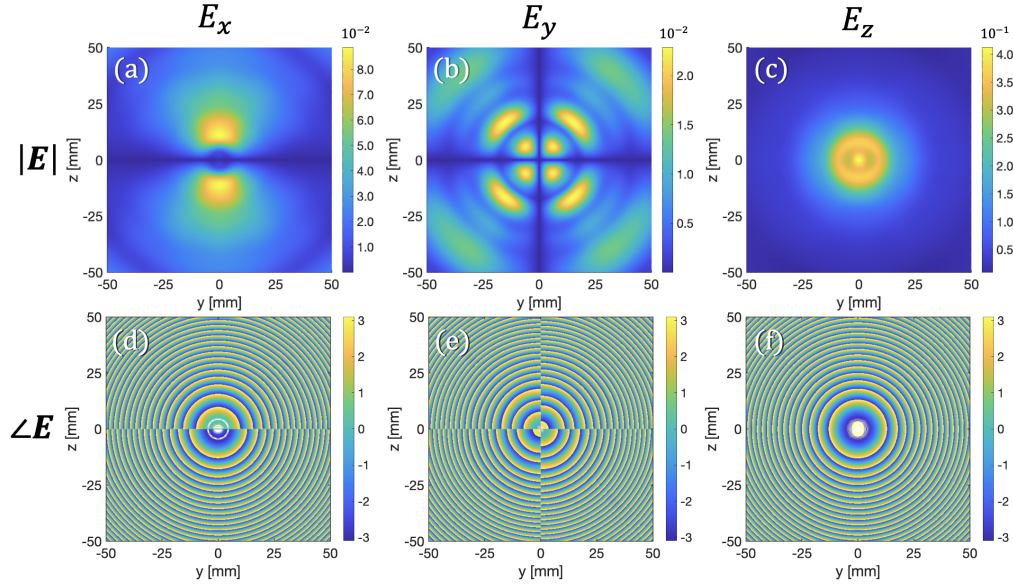


Fig. 9. The scattering simulation from the multilayered spherical structure with 3D ASM method at 175 GHz. Subfigures a)-c) presents the magnitudes, and d)-f) present the phases of the Cartesian components at the transverse plane at 40 mm from the origin of the cornea. The cornea was modeled as 50-layer structure.

an excellent match down to less than -38 dB difference to the change calculated from a similar multilayered stratified medium structure, i.e., 50 layered planar surfaces illuminated with the plane wave. This comparison was made as $E_{3DASM_{scat.}}/E_{3DASM_{inc.}} - E_{PW_{scat.}}/E_{PW_{inc.}}$. The plane-wave illumination to the planar surface gives the reference scattering, which is used to evaluate the thickness and CTWC of the cornea.

The coupling coefficient K between the incident and scattered fields plays a critical role in the cornea's CTWC and thickness analysis. In this analysis, the obtained K in the observed frequency range is fitted to match the cornea's CTWC- and thickness-dependent reflectivity curve from the planar reference structure. In this paper, the K from the cornea model was calculated with two different illumination scenarios in the 200 GHz - 400 GHz band; by the field synthesized from the spherical top-hat field distribution and by the Gaussian beam, whose frequency-dependent waist was located at the origin of the cornea [8]. Obtained values were compared to the reference values, i.e, plane-wave illumination of the planar layered structure with the same layer thickness and permittivity values, see Figure 10. The K of the equal phase top-hat distribution indicates a high match with amplitude less than 0.8% and tapered top-hat less than 0.7% average difference compared to the reference plane wave scenario. Typical Gaussian-beam illumination produces a 4-5% amplitude difference. This improved matching in K cut down the fitting errors in the cornea's CTWC and thickness analysis. It is also worthwhile to mention that the total reflected energy of the beam with the spherical tapered and untapered top-hat distribution matches with less than 0.07% average difference compared to the plane wave scenario, thus we can conclude that the small difference in the K magnitude of the top-hat beam and reference values are due to the differences in the diffraction patterns between the incident and scattered fields.

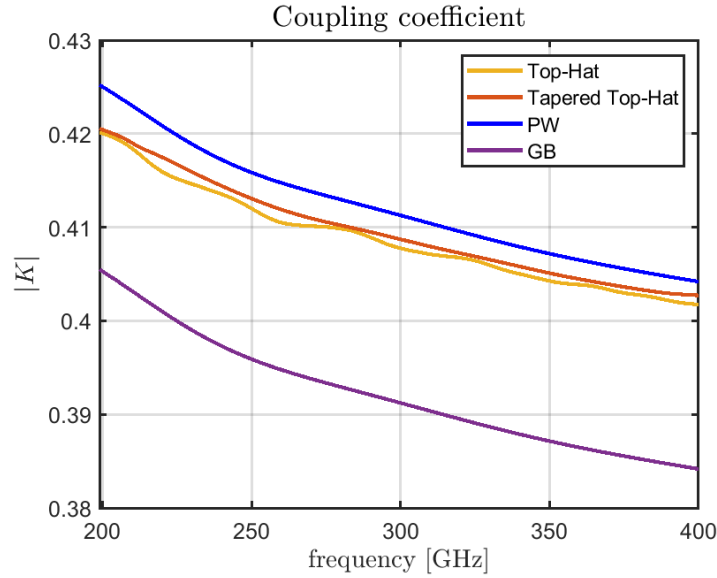


Fig. 10. The magnitude of the coupling coefficient from 200 to 400 GHz frequency range in four scenarios. The blue line presents the reference value from plane wave illumination into the planar structure, the red line presents the top-hat illumination, the yellow line presents tapered top-hat illumination, and the purple line presents the typical Gaussian beam illumination for spherical structure.

4. Conclusions

This paper proposes a novel method for expanding the nominally planar AS method to synthesize incident electromagnetic beams from electric field distributions on spherical surfaces. The derivation of the method was presented, and the resulting equations were proved mathematically in Appendix A. The proposed method can be expanded to synthesize beams from the arbitrary smooth surfaces taking the radii of curvatures and frequency range into account. The minimum radius of curvature of the surface compared to the wavelength is $RoC > 2\lambda$. The benefit of this method is the ability to present the synthesized fields in the angular spectrum domain, which can be used to compute the VSH coefficients of the incident fields. Thus the incident field can be presented with VSH expansion and scattered fields from multilayered spherical structures, of an arbitrarily large number of layers, can be obtained utilizing the Mie theory. The computational effort of presented 50-layer spherical scattering simulations requires much less memory and fewer arithmetical operations than, for example, similar full-wave computation.

First, the advantages of the beams with spherically matching wavefronts compared to the Gaussian beam illumination for spherical objects were presented. This was done by comparing the scattering behavior of the top-hat, tapered top-hat and Gaussian beam illumination from the spherical 27-layer bandpass filter. These results were compared to the reference scattering from interaction with plane wave and planar 27-layer bandpass filter. The beams with spherically matching wavefront had significantly increased coupling coefficient compared to the traditional Gaussian beam illumination. Next, the Cartesian components of the incident field were evaluated at the transverse plane at 40 mm from the origin of the cornea. These results were compared to the physical optics simulations and demonstrated good agreement. Then the gradient permittivity of the cornea was modeled as a multilayered spherical structure of 50 layers, and the scattered beam was evaluated from the ideal incident field with a spherical top-hat and tapered top-hat wavefront by the T-matrix method. The coupling coefficients between the incident and scattered

fields of the spherical top-hat distributions were evaluated in the 200 GHz to 400 GHz region and compared to Gaussian-beam illumination and the reference plane-wave illumination on an analog planar surface. The coupling coefficient amplitude of the spherical tapered top-hat illumination was closest to the reference amplitude with less than 0.7% average difference. The good agreement between the coupling coefficient and the reference validates the proposed method. The results indicate that the incident beam with a matching spherical wavefront interacts with the multilayered sphere similar to the plane wave interacting with the planar structures. Thus, the developed method enables the synthesis of beams whose interaction with the cornea can be more accurately predicted/analyzed with standard EMT and SMT and improves the accuracy of CTWC and thickness measurement in THz band.

The presented method will enable the computation of electric field propagation between different surfaces. The desired incident field can be synthesized from the cornea's surface distribution as presented in this paper and computed at the optical elements. This electric field distribution at the optical element can then be used as a source distribution and propagated back to the cornea. Through this methodology, the minimum optical element apertures can be evaluated by comparing the surface field distribution from the propagated field to the original surface distribution.

5. Appendix A

Theorem 5.1. *Let the function E_0 be continuous in a closed segment of sphere Ω and let $\mathbf{r} \in \mathbb{R}^3$ be such that $\mathbf{r} \cdot \mathbf{n} \neq 1$ for all $\mathbf{n} \in \Omega$. The field E created by function E_0 is presented by (15) and (16) at point \mathbf{r} , where \bar{x} , \bar{y} and \bar{z} are as in (6).*

Proof. Let us define $\epsilon > 0$. Let us show first, that when the partition Ω_t is small enough, in other words, the areas $|\Omega_t|$ are small enough regardless of t , by replacing the function E_0^t supported by each piece Ω_t with a constant $E_0^t(\bar{0}, \bar{0}) = E_0(\theta, \phi)$, the error made in formula (10) is smaller than $\epsilon/4$. Function E_0 is uniformly continuous on the compact segment of sphere Ω , and based on this, with sufficiently small $|\Omega_t|$ it holds

$$|E_0^t(\bar{x}, \bar{y}) - E_0(\theta, \phi)| \leq \frac{\epsilon}{4I|\Omega|} \quad (31)$$

for all $\bar{x}, \bar{y} \in \Omega_t$ and t , where the constant I will be defined later on. In the Fourier transform (7) on the plane holds

$$\begin{aligned} |\mathcal{F}\{E_0^t\} - \mathcal{F}\{E_0(\theta, \phi)\}| &\leq \iint_{\Omega_t} |E_0^t(\bar{x}, \bar{y}) - E_0(\theta, \phi)| |e^{-i(k_{\bar{x}}\bar{x} + k_{\bar{y}}\bar{y})}| d\bar{x}d\bar{y} \\ &\leq \iint_{\Omega_t} \frac{\epsilon}{4I|\Omega|} |e^{-i(k_{\bar{x}}\bar{x} + k_{\bar{y}}\bar{y})}| d\bar{x}d\bar{y} \leq \iint_{\Omega_t} \frac{\epsilon}{4I|\Omega|} d\bar{x}d\bar{y} = \frac{\epsilon|\Omega_t|}{4I|\Omega|}, \end{aligned} \quad (32)$$

for all $(k_{\bar{x}}, k_{\bar{y}}) \in \mathbb{R}^2$. Function $e^{i|\bar{z}|\sqrt{k^2 - k_{\bar{x}}^2 - k_{\bar{y}}^2}}$ is integrable on $(k_{\bar{x}}, k_{\bar{y}})$ plane, because outside of the circle $k_{\bar{x}}^2 + k_{\bar{y}}^2 = k^2$, the exponential becomes real and negative. Let I be at first a continuous elementary function

$$I(|\bar{z}|) = \iint_{\mathbb{R}^2} |e^{i|\bar{z}|\sqrt{k^2 - k_{\bar{x}}^2 - k_{\bar{y}}^2}}| dk_{\bar{x}} dk_{\bar{y}}, \quad (33)$$

where $\bar{z} = \bar{z}(\theta, \phi)$; see (6). A continuous function $|\bar{z}(\theta, \phi)|$ gets its minimum value $\bar{z}_{min} > 0$ on the compact set $\{(\theta, \phi) | \theta \in [0, \theta_0], \phi \in [0, 2\pi]\}$. Especially $|\bar{z}| \geq \bar{z}_{min}$ for all t regardless of partitioning. Finally, the constant I is defined

$$I = I(\bar{z}_{min}) < \infty. \quad (34)$$

Due the monotone of integral, $I(|\bar{z}(\theta, \phi)|) \leq I$ on all t regardless of partitions. The upper limit for the error due $E_0(\theta, \phi)$ on the formula (12) is obtained as

$$\begin{aligned}
& \frac{1}{4\pi^2} \iint_{\mathbb{R}^2} |\mathcal{F}\{E'_0\} - \mathcal{F}\{E_0(\theta, \phi)\}|(k_{\bar{x}}, k_{\bar{y}})|e^{i|\bar{z}|\sqrt{k^2 - k_{\bar{x}}^2 - k_{\bar{y}}^2}}|dk_{\bar{x}}dk_{\bar{y}} \\
& \leq \frac{1}{4\pi^2} \frac{\epsilon|\Omega_t|}{47|\Omega|} \iint_{\mathbb{R}^2} |e^{i|\bar{z}|\sqrt{k^2 - k_{\bar{x}}^2 - k_{\bar{y}}^2}}|dk_{\bar{x}}dk_{\bar{y}} \\
& \leq \frac{1}{4\pi^2} \frac{\epsilon|\Omega_t|}{47|\Omega|} I \leq \frac{\epsilon|\Omega_t|}{4|\Omega|},
\end{aligned} \tag{35}$$

where (31) and (34) have been used. Because of $\|\mathbf{e}_\theta\| = 1$ and the triangle inequality the error in formula (13) is

$$err_1 \leq \sum_t \frac{\epsilon|\Omega_t|}{4|\Omega|} = \frac{\epsilon}{4}. \tag{36}$$

In the above approximation, a constant $E_0(\theta, \phi)$ is used on piece Ω ; as a function it is zero on the plane outside of the piece, let us denote this function simply as $E_0(\theta, \phi)$. Next, we consider the Fourier transform of function $E_0(\theta, \phi)$. Because function $e^{i|\bar{z}|\sqrt{k^2 - k_{\bar{x}}^2 - k_{\bar{y}}^2}}$ is integrable, there can be found an origin centered closed disk \bar{B} such that

$$[\max_{\Omega}|E_0|] \iint_{\mathbb{R}^2/\bar{B}} |e^{i|\bar{z}|\sqrt{k^2 - k_{\bar{x}}^2 - k_{\bar{y}}^2}}|dk_{\bar{x}}dk_{\bar{y}} < \frac{\epsilon}{4|\Omega|} \tag{37}$$

for all t because $|\bar{z}| \geq \bar{z}_{min}$. For all $(k_{\bar{x}}, k_{\bar{y}}) \in \mathbb{R}^2$ it holds

$$\begin{aligned}
& |\mathcal{F}\{E_0(\theta, \phi)\}(k_{\bar{x}}, k_{\bar{y}})| \\
& \leq [\max_{\Omega}|E_0|] \iint_{\Omega_t} 1dk_{\bar{x}}dk_{\bar{y}} = \max|E_0||\Omega_t|.
\end{aligned} \tag{38}$$

Let us now consider the error (err_2) made in integral (12) when $\mathcal{F}\{E_0(\theta, \phi)\}$ is replaced by the constant $E_0(\theta, \phi)|\Omega_t|$. Under estimates (37) and (38) it follows

$$\begin{aligned}
& \iint_{\mathbb{R}^2/\bar{B}} |\mathcal{F}\{E_0(\theta, \phi)\} - E_0(\theta, \phi)|\Omega_t||e^{i|\bar{z}|\sqrt{k^2 - k_{\bar{x}}^2 - k_{\bar{y}}^2}}|dk_{\bar{x}}dk_{\bar{y}} \\
& \leq \iint_{\mathbb{R}^2/\bar{B}} 2[\max_{\Omega}|E_0|]|\Omega_t||e^{i|\bar{z}|\sqrt{k^2 - k_{\bar{x}}^2 - k_{\bar{y}}^2}}|dk_{\bar{x}}dk_{\bar{y}} \\
& \leq 2|\Omega_t|\frac{\epsilon}{4|\Omega|} = \frac{\epsilon|\Omega_t|}{2|\Omega|}.
\end{aligned} \tag{39}$$

For all $(k_{\bar{x}}, k_{\bar{y}}) \in \bar{B}$ and $(\bar{x}, \bar{y}) \in \Omega_t$, we can estimate by continuity of the function

$$[\max_{\Omega}|E_0|] |e^{-i(k_{\bar{x}}\bar{x} + k_{\bar{y}}\bar{y})} - 1| \leq \frac{\epsilon}{4|\bar{B}||\Omega|} \tag{40}$$

always when $|\Omega_t|$ is small enough, because then $\bar{x} \approx 0$, $\bar{y} \approx 0$ and hence $k_{\bar{x}}\bar{x} + k_{\bar{y}}\bar{y} \approx 0$ – that is the assignment of \bar{B} . Then in the Fourier transform at point $(k_{\bar{x}}, k_{\bar{y}}) \in \bar{B}$ it holds

$$\begin{aligned}
& |\mathcal{F}\{E_0(\theta, \phi)\}(k_{\bar{x}}, k_{\bar{y}}) - E_0(\theta, \phi)|\Omega_t|| \\
& = \left| \iint_{\Omega_t} E_0(\theta, \phi)e^{-i(k_{\bar{x}}\bar{x} + k_{\bar{y}}\bar{y})}d\bar{x}d\bar{y} - E_0(\theta, \phi)1d\bar{x}d\bar{y} \right| \\
& \leq |E_0(\theta, \phi)| \iint_{\Omega_t} |e^{-i(k_{\bar{x}}\bar{x} + k_{\bar{y}}\bar{y})} - 1|d\bar{x}d\bar{y} \\
& \leq \iint_{\Omega_t} \frac{\epsilon}{4|\bar{B}||\Omega|}d\bar{x}d\bar{y} = \frac{\epsilon|\Omega_t|}{4|\bar{B}||\Omega|}.
\end{aligned} \tag{41}$$

Replacing by $\mathcal{F}\{E_0(\theta, \phi)\}$ with the constant $E_0(\theta, \phi)|\Omega_t|$ in formula (12) we make an error

$$\begin{aligned}
& \frac{1}{4\pi^2} \left(\iint_{\bar{B}} + \iint_{\mathbb{R}^2/\bar{B}} \right) |\mathcal{F}\{E_0(\theta, \phi)\} - E_0(\theta, \phi)|\Omega_t||e^{i|\bar{z}|\sqrt{k^2 - k_{\bar{x}}^2 - k_{\bar{y}}^2}}|dk_{\bar{x}}dk_{\bar{y}} \\
& \leq \frac{\epsilon|\Omega_t|}{4|\bar{B}||\Omega_t|} \iint_{\bar{B}} 1dk_{\bar{x}}dk_{\bar{y}} + \frac{\epsilon|\Omega_t|}{2|\Omega|} = \frac{\epsilon|\Omega_t|}{4|\Omega|} + \frac{\epsilon|\Omega_t|}{2|\Omega|} = \frac{3\epsilon|\Omega_t|}{4|\Omega|},
\end{aligned} \tag{42}$$

where the estimates (39) and (41) have been used. The error for sum (13) is obtained as

$$err_2 \leq \sum_t \frac{3\epsilon |\Omega_t|}{4|\Omega|} = \frac{3\epsilon}{4}. \quad (43)$$

Thus, when the partition Ω_t is dense enough and $\mathbf{r} \in \mathbb{R}^3$ be such that $\mathbf{r} \cdot \mathbf{n} \neq 1$ for all $\mathbf{n} \in \Omega$, we get by (36) and (43)

$$\begin{aligned} & \left\| \sum_t E_t(\mathbf{r}) \mathbf{e}_\theta - \frac{1}{4\pi^2} \sum_t E_0(\theta, \phi) \mathbf{e}_\theta(\theta, \phi) |\Omega_t| \iint_{\mathbb{R}} e^{i(k_{\bar{x}} \bar{x} + k_{\bar{y}} \bar{y})} e^{i|\bar{z}| \sqrt{k^2 - k_{\bar{x}}^2 - k_{\bar{y}}^2}} dk_{\bar{x}} dk_{\bar{y}} \right\| \\ & \leq err_1 + err_2 \leq \frac{\epsilon}{4} + \frac{3\epsilon}{4} = \epsilon. \end{aligned} \quad (44)$$

Finally, by continuity of the integrand, the integral in (15) exists, and, because of the estimate (44), for the points $\mathbf{r} \in \mathbb{R}^3$ like in Theorem there also exists

$$\begin{aligned} \mathbf{E}_\theta(\mathbf{r}) &= \mathbf{E}_\theta(x, y, z) = \lim_{|\Omega_t| \rightarrow 0} \sum_t E_t(\mathbf{r}) \mathbf{e}_\theta \\ &= \frac{1}{4\pi^2} \iint_{\Omega} E_0(\theta, \phi) \mathbf{E}_t(\mathbf{r}; \theta, \phi) \sin \theta d\theta d\phi. \end{aligned} \quad (45)$$

□

The proof above is also valid for the sum of the second vector component of (19). Only a few modifications are needed.

6. Appendix B

The VSH beam shape coefficients for each ij - plane wave of the incident field is defined as [33]

$$\begin{aligned} a_{\text{emn}ij}^t &= 4i^n \mathbf{e}_{oij} \cdot \left[-\mathbf{e}_\theta \sin(m\phi) \frac{m}{\sin \theta} P_n^m(\cos \theta) - \mathbf{e}_\phi \cos(m\phi) \frac{d}{d\theta} P_n^m(\cos \theta) \right], \\ a_{\text{omn}ij}^t &= 4i^n \mathbf{e}_{oij} \cdot \left[\mathbf{e}_\theta \cos(m\phi) \frac{m}{\sin \theta} P_n^m(\cos \theta) - \mathbf{e}_\phi \sin(m\phi) \frac{d}{d\theta} P_n^m(\cos \theta) \right], \\ b_{\text{emn}ij}^t &= -4i^{n+1} \mathbf{e}_{oij} \cdot \left[\mathbf{e}_\theta \cos(m\phi) \frac{m}{\sin \theta} P_n^m(\cos \theta) - \mathbf{e}_\phi \sin(m\phi) \frac{d}{d\theta} P_n^m(\cos \theta) \right], \\ b_{\text{omn}ij}^t &= -4i^{n+1} \mathbf{e}_{oij} \cdot \left[\mathbf{e}_\theta \sin(m\phi) \frac{m}{\sin \theta} P_n^m(\cos \theta) + \mathbf{e}_\phi \cos(m\phi) \frac{d}{d\theta} P_n^m(\cos \theta) \right], \end{aligned} \quad (46)$$

where P_n^m is the associated Legendre function of the first kind of degree n and order m . The scattered field from differential element in VSH presentation is obtained as

$$\begin{aligned} \mathbf{E}_{\text{scat}}(k\mathbf{r}) &= p^2 \sum_m \sum_n D_{mn} \left[f_{\text{emn}} \mathbf{M}_{\text{emn}}^{(3)}(k\bar{\mathbf{r}}) + f_{\text{omn}} \mathbf{M}_{\text{omn}}^{(3)}(k\bar{\mathbf{r}}) \right. \\ & \quad \left. + g_{\text{emn}} \mathbf{N}_{\text{emn}}^{(3)}(k\bar{\mathbf{r}}) + g_{\text{omn}} \mathbf{N}_{\text{omn}}^{(3)}(k\bar{\mathbf{r}}) \right], \end{aligned} \quad (47)$$

where the superscripts (3) presents the vectors spherical harmonics (outgoing wave) with spherical Hankel function of the first kind $h_n^{(1)}(kr)$. The f_{emn} , f_{omn} , g_{emn} and g_{omn} are vector spherical harmonic coefficient for the scattered field calculated from the T-matrix method as

$$\begin{bmatrix} f_{\text{emn}} \\ f_{\text{omn}} \\ g_{\text{emn}} \\ g_{\text{omn}} \end{bmatrix} = \begin{bmatrix} T_{11} & 0 & 0 & 0 \\ 0 & T_{22} & 0 & 0 \\ 0 & 0 & T_{33} & 0 \\ 0 & 0 & 0 & T_{44} \end{bmatrix} \begin{bmatrix} a_{\text{emn}} \\ a_{\text{omn}} \\ b_{\text{emn}} \\ b_{\text{omn}} \end{bmatrix}, \quad (48)$$

where the T-matrix elements for the multilayered sphere is obtained by the algorithm defined in [34]. The coupling coefficient between the incident and scattered field can be obtained as

$$K = \frac{\int \int [\mathbf{E}_{inc} \cdot \mathbf{E}_{sca}] dx dy}{\int \int [\mathbf{E}_{inc} \cdot \mathbf{E}_{inc}^*] dx dy}, \quad (49)$$

where \mathbf{E}_{inc} and \mathbf{E}_{sca} are computed by Eq. (29) and Eq. (30), and * denotes the complex conjugate.

Funding. This research was supported by Academy of Finland #327640: Assessment of the Graft Rejection Using Millimeter Waves (AGRUM) and the Agencia Estatal Investigación PID2019-107885GB-C31/AEI/10.13039, PRE2018-084326.

Disclosures. The authors declare no conflicts of interest.

Data availability. Data underlying the results presented in this paper are not publicly available at this time but may be obtained from the authors upon reasonable request.

References

1. Y. Deng and X. Liu, "Electromagnetic imaging methods for nondestructive evaluation applications," *Sensors* **11**, 11774–11808 (2011).
2. X. Liu and D. Zhao, "The statistical properties of anisotropic electromagnetic beams passing through the biological tissues," *Opt. Commun.* **285**, 4152 – 4156 (2012).
3. P. Sowa, J. Rutkowska-Talipska, U. Sulkowska, K. Rutkowski, and R. Rutkowski, "Electromagnetic radiation in modern medicine: Physical and biophysical properties," *Pol. Annals Medicine* **19**, 139 – 142 (2012).
4. Z. D. Taylor, J. Garritano, S. Sung, N. Bajwa, D. B. Bennett, B. Nowroozi, P. Tewari, J. Sayre, J. P. Hubschman, S. Deng, E. R. Brown, and W. S. Grundfest, "Thz and mm-wave sensing of corneal tissue water content: Electromagnetic modeling and analysis," *IEEE Transactions on Terahertz Sci. Technol.* **5**, 170–183 (2015).
5. D. B. Bennett, Z. D. Taylor, P. Tewari, R. S. Singh, M. O. Culjat, W. S. G. M.D., D. J. Sassoon, R. D. Johnson, J.-P. Hubschman, and E. Brown, "Terahertz sensing in corneal tissues," *J. Biomed. Opt.* **16**, 1 – 9 (2011).
6. N. W. Bergmann, D. Abbott, A. Hariz, and V. K. Varadan, eds., *Electronics and Structures for MEMS II*, vol. 4591 (SPIE, 2001).
7. P. Y. Han, G. C. Cho, and X.-C. Zhang, "Time-domain transillumination of biological tissues with terahertz pulses," *Opt. Lett.* **25**, 242–244 (2000).
8. A. Tamminen, S. V. Pälli, J. Ala-Laurinaho, M. Salkola, A. V. Räisänen, and Z. D. Taylor, "Quasioptical system for corneal sensing at 220–330 ghz: Design, evaluation, and ex vivo cornea parameter extraction," *IEEE Transactions on Terahertz Sci. Technol.* **11**, 135–149 (2021).
9. F. Zarrinkhat, J. Lamberg, A. Tamminen, M. Baggio, J. Ala-Laurinaho, E. E. M. Khaled, J. M. Rius, J. R. Robert, and Z. Taylor, "Fourier analysis of submillimeter-wave scattering from the human cornea," in *2021 15th European Conference on Antennas and Propagation (EuCAP)*, (2021), pp. 1–5.
10. P. Yeh, A. Yariv, and C.-S. Hong, "Electromagnetic propagation in periodic stratified media. i. general theory*," *J. Opt. Soc. Am.* **67**, 423–438 (1977).
11. G. A. Niklasson, C. G. Granqvist, and O. Hunderi, "Effective medium models for the optical properties of inhomogeneous materials," *Appl. Opt.* **20**, 26–30 (1981).
12. M. Gharghi, H. Bai, G. Stevens, and S. Sivoththaman, "Modeling and simulation of spherical solar cells," in *Conference Record of the Thirty-first IEEE Photovoltaic Specialists Conference, 2005.*, (2005), pp. 1177–1180.
13. N. Keerativoranan, P. Hanpinitasak, K. Saito, and J. I. Tadaka, "Circular mesh based physical optics for scattered field prediction," *IEEE Antennas Wirel. Propag. Lett.* pp. 1–1 (2021).
14. J. R. Sanford, "Scattering by spherically stratified microwave lens antennas," *IEEE Transactions on Antennas Propag.* **42**, 690–698 (1994).
15. G. Gouesbet, J. Lock, and G. Gréhan, "Generalized lorenz–mie theories and description of electromagnetic arbitrary shaped beams: Localized approximations and localized beam models, a review," *J. Quant. Spectrosc. Radiat. Transf.* **112**, 1–27 (2011).
16. C. Bohren and D. R. Huffman, *Absorption and Scattering of Light by Small Particles* (Wiley Science Paperback Series, 1998).
17. J. W. Goodman, *Introduction to Fourier optics* (Englewood, CO: Roberts, 2005).
18. E. E. M. Khaled, S. C. Hill, and P. W. Barber, "Scattered and internal intensity of a sphere illuminated with a gaussian beam," *IEEE Transactions on Antennas Propag.* **41**, 295–303 (1993).
19. C.-Y. Hwang, S. Oh, I.-K. Jeong, and H. Kim, "Stepwise angular spectrum method for curved surface diffraction," *Opt. Express* **22**, 12659–12667 (2014).
20. L. Ebers, M. Hammer, and J. Förstner, "Light diffraction in slab waveguide lenses simulated with the stepwise angular spectrum method," *Opt. Express* **28**, 36361–36379 (2020).

21. N. G. Worku, R. Hambach, and H. Gross, "Decomposition of a field with smooth wavefront into a set of gaussian beams with non-zero curvatures," *J. Opt. Soc. Am. A* **35**, 1091–1102 (2018).
22. J.-S. Lee, T.-L. Song, J.-K. Du, and J.-G. Yook, "Near-field to far-field transformation based on stratton-chu fomula for emc measurements," in *2013 IEEE Antennas and Propagation Society International Symposium (APSURSI)*, (2013), pp. 606–607.
23. J. Lamberg, F. Zarrinkhat, A. Tamminen, E. E. M. Khaled, and Z. Taylor, "Investigation of radial top-hat electric field distributions for corneal reflectometry using modified fourier optics method," in *2021 46th International Conference on Infrared, Millimeter and Terahertz Waves (IRMMW-THz)*, (2021), pp. 1–2.
24. W. C. Chew, *Planarly Layered Media* (1995), pp. 45–160.
25. W. Hsu and R. Barakat, "Stratton–chu vectorial diffraction of electromagnetic fields by apertures with application to small-fresnel-number systems," *J. Opt. Soc. Am. A* **11**, 623–629 (1994).
26. E. E. M. Khaled, S. C. Hill, and P. W. Barber, "Light scattering by a coated sphere illuminated with a gaussian beam," *Appl. Opt.* **33**, 3308–3314 (1994).
27. L. N. Trefethen and J. A. C. Weideman, "The exponentially convergent trapezoidal rule," *SIAM Rev.* **56**, 385–458 (2014).
28. M. A. Butt, S. A. Fomchenkov, and S. N. Khonina, "Multilayer dielectric stack notch filter for 450-700 nm wavelength spectrum," (2017).
29. F. Zarrinkhat, J. Lamberg, A. Tamminen, M. Baggio, I. Nefedova, J. Ala-Laurinaho, E. E. M. Khaled, J. Rius, J. Romeu, and Z. Taylor, "Vector spherical harmonic analysis and experimental validation of spherical shells illuminated with broadband, millimeter wave gaussian beams: applications to corneal sensing," *Biomed. Opt. Express* **13**, 3699–3722 (2022).
30. F. Zarrinkhat, M. Baggio, J. Lamberg, A. Tamminen, I. Nefedova, J. Ala-Laurinaho, E. E. M. Khaled, J. M. Rius, J. Romeu, and Z. Taylor, "Calibration alignment sensitivity in corneal terahertz imaging," *Sensors* **22** (2022).
31. A. Tamminen, M. Baggio, I. Nefedova, Q. Sun, S. Presnyakov, J. Ala-laurinaho, E. Brown, V. Wallace, E. Macpherson, T. Maloney, N. Kravchenko, M. Salkola, S. Deng, and Z. Taylor, "Extraction of thickness and water content gradients in hydrogel-based, water-backed corneal phantoms via submillimeter wave reflectometry," *IEEE Transactions on Terahertz Sci. Technol.* pp. 1–1 (2021).
32. J. T. Kindt and C. A. Schmuttenmaer, "Far-infrared dielectric properties of polar liquids probed by femtosecond terahertz pulse spectroscopy," *The J. Phys. Chem.* **100**, 10373–10379 (1996).
33. P. W. Barber and S. C. Hill, *Light Scattering By Particles: Computational Methods* (Advanced Series in Applied Physics, 1990).
34. U. P. O. Peña, "Scattering of electromagnetic radiation by a multilayered sphere," *IEEE Antennas Propag. Mag.* **57**, 69–116 (2015).